Earth and Planetary Science Letters 416 (2015) 91–97

Contents lists available at ScienceDirect

Earth and Planetary Science Letters

www.elsevier.com/locate/epsl

Velocity contrast along the rupture zone of the 2010 Mw6.9 Yushu, China, earthquake from fault zone head waves

Wei Yang [a], Zhigang Peng [b,*], Baoshan Wang [a], Zefeng Li [b], Songyong Yuan [a]

[a] Key Laboratory of Seismic Observation and Geophysical Imaging, Institute of Geophysics, CEA, Beijing, China
[b] School of Earth and Atmospheric Sciences, Georgia Institute of Technology, Atlanta, GA, USA

ARTICLE INFO

Article history:
Received 25 October 2014
Received in revised form 27 January 2015
Accepted 31 January 2015
Available online 26 February 2015
Editor: P. Shearer

Keywords:
bimaterial interface
Garzê–Yushu Fault
fault zone head waves
velocity contrast
low-velocity zone

ABSTRACT

Fault zone head waves (FZHWs) travel along the bimaterial fault interface and can be used to provide high-resolution imaging of fault zone properties. Here we use aftershock data following the 2010/04/13 Mw6.9 Yushu earthquake to quantify velocity contrast along the Garzê–Yushu Fault (GYF). FZHWs are identified as low-amplitude, long-period seismic signals with polarities opposite to the direct P arrivals. We observe FZHWs at 4 stations near faults that bound both sides of the Jielong basin, which is a pull-apart basin that is partially filled by Longbao Lake. The time delays between the direct P and FZHWs increase systematically with along-strike distances, and the corresponding observed velocity contrast is on the order of 5–8%. However, we do not observe a clear increase of time delay with hypocentral depth, suggesting that the pull-apart basin forms a thick low-velocity zone that likely exists in the top few kilometers of the crust. The velocity contrast southeast of the mainshock epicenter is very small (1–3%), consistent with both field observations and seismic tomographic results.

1. Introduction

Lithological contrasts across major faults often result in sharp bimaterial interfaces, which may lead to significant differences in seismic radiation and propagation. As an example, seismic waves can refract along such an interface with the seismic velocity (and first motion polarity) of the faster side, and then radiate from the fault to the slower side. Beyond a critical distance, the refracted waves, also known as the fault zone head waves (FZHWs), arrive earlier than the direct waves and are characterized by an emergent waveform with opposite first-motion polarity to that of the direct waves (e.g., Ben-Zion and Malin, 1991). Since FZHWs spend most of times propagating along the fault interface, they can be used to provide additional important constraints on the velocity contrast at seismogenic depth.

FZHWs have been observed along several major plate boundary faults. These include the San Andreas Fault (SAF) at Parkfield (e.g., Ben-Zion and Malin, 1991; Zhao et al., 2010) and south of Hollister (e.g., McGuire and Ben-Zion, 2005; Lewis et al., 2007), the Calaveras Fault (e.g., Zhao and Peng, 2008) and the Hayward Fault in the Bay area (e.g., Allam et al., 2014), and the North Anatolian Fault (NAF) in northwestern Turkey (e.g., Bulut et al., 2012; Najdahmadi et al., 2014). FZHWs can also be generated along velocity contrast interfaces away from plate boundaries (e.g., Hough et al., 1994). Another such case is discussed in this paper, where we conduct a systematic search for FZHWs along the Garzê–Yushu Fault (GYF) that ruptured during the 2010 Mw6.9 Yushu earthquake (Fig. 1).

We choose this region mainly because of the abundant aftershock data collected by a temporary network (Section 2). In addition, recent tomographic studies have also revealed clear evidence of velocity contrasts down to ~10 km depth in this region (e.g., Wang et al., 2013). In the following sections, we first introduce the tectonic setting of the study region and the seismic deployment, followed by a detailed description of the analysis procedure. We then present evidence for FZHWs in this region and estimate the velocity contrast. Finally, we discuss implications of the observed velocity contrasts and their possible relationship with earthquake rupture properties.

2. Study region and seismic data

The GYF is a left-lateral strike-slip fault that separates the Bayan Har block (the northeast side, NE) and the Qiangtang block (the southwest side, SW) in eastern Tibetan Plateau (Fig. 1). The Holocene sinistral slip rate of this fault is estimated to be 7.3–12 mm/yr along the Yushu segment of the GYF (e.g., Zhou and Ma, 1996; Wen et al., 2003). The western fault segment of the GYF

* Corresponding author.
E-mail address: zpeng@gatech.edu (Z. Peng).

http://dx.doi.org/10.1016/j.epsl.2015.01.043
0012-821X/

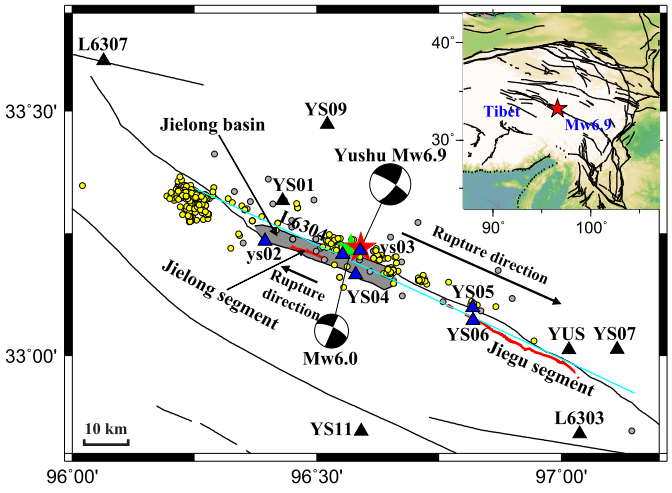

Fig. 1. A map of the study region around the Mw6.9 Yushu mainshock. The epicenters of the 2010 Mw6.9 Yushu earthquake and its largest aftershock (Mw6.0) are marked as stars with red and green colors, respectively. The focal mechanisms are from the Global Centroid Moment Tensor catalog (http://www.globalcmt.org). The solid black lines denote the faults in this region, the red solid lines denote the mainshock surface rupture zone along the GYF (e.g., Guo et al., 2012), the gray area denotes the Jielong basin (e.g., Wang et al., 2008), and the cyan solid line marks the simplified fault interface (strike 294.95°) used in this study. The seismic stations are shown as triangles with the blue colors denoting stations that record FZHWs. Aftershocks with FZHWs are marked as yellow (relocated catalog) or gray (original catalog) circles. The inset shows a larger map of the Tibet plateau (For interpretation of the references to color in this figure legend, the reader is referred to the web version of this article.).

consists of two active fault branches (*a left-step-over*) that bound of the Jielong basin (Fig. 1), a pull-apart basin produced by the left-step-over part of the GYF, and partially filled by Longbao Lake (e.g., Wang et al., 2008).

Since the beginning of the 20th century, more than 10 earthquakes with Ms $\geq$ 7.0 have occurred around the Bayan Har block (e.g., Chen et al., 2010), including the 2008 Mw7.9 (Ms8.0) Wenchuan earthquake near the boundary with the Sichuan basin. Another major event is an Mw6.9 earthquake that ruptured the Yushu segment of the GYF in April 2010, with its epicenter at ~40 km west of Jiegu Town, Yushu County, Qinghai Province, China. The mainshock and its largest aftershock (Mw6.0) resulted in a ~70 km long rupture zone striking 310°–320° (e.g., Chen et al., 2010; Li et al., 2012; Xu et al., 2013). The surface rupture (Fig. 1) can be divided into two segments: the ~15 km long Jielong segment northwest of the mainshock epicenter, and the ~30 km long Jiegu segment southeast of the epicenter. In the middle is the pull-apart Jielong basin.

Wang and Mori (2012) analyzed waveforms recorded by a permanent station YUS near Jiegu Town and teleseismic stations, and suggested that part of the mainshock rupture to the southeast was supershear (i.e., rupture velocity faster than the local shear wave velocity). This may partially explain the severe damage at Jiegu Town, which is located in the forward direction of the rupture front. Based on joint inversion of teleseismic and InSAR datasets, Yokota et al. (2012) also found similar evidence of supershear rupture. In addition, Zhang et al. (2013) performed similar joint inversions but found no supportive evidence of supershear rupture.

About 20 days after the mainshock, scientists from the China Earthquake Administration (CEA) deployed 26 temporary seismic stations around the mainshock rupture zone to monitor subsequent aftershocks. In particular, 10 stations (9 temporary stations and YUS permanent station) were located on both sides of the GYF (Fig. 1). Each temporary seismic station consisted of a RefTek-130B digitizer and a Guralp-3ESPC three-component broadband seismometer with flat frequency response from 0.016 (60 s) to 50 Hz. The permanent YUS station has a three-component KS2000 broadband seismometer with a flat frequency response from 0.0083 (120 s) to 50 Hz. The sampling rate of both temporary and permanent stations is 100 samples/s. During the observation period (May 2010 to November 2010), up to ~2000 aftershocks were recorded (e.g., Wang et al., 2013, 2014), which provides a rich dataset for imaging detailed fault zone structures in this region.

3. Analysis procedure

The analysis procedure generally follows those described in previous FZHW studies (e.g., Zhao et al., 2010; Allam et al., 2014). We first select 10 seismic stations (Fig. 1) on both sides of the GYF (Table S1). Next, we select events that were recorded with relatively high signal to noise ratio (SNR), and then manually pick the arrivals of the direct *P* waves. To avoid potential contamination of the FZHWs from applying a digital filter, we only remove the mean but do not apply any additional filter on the data (e.g., Allam et al., 2014). Because FZHWs are fundamentally emergent phases and hence produce less high frequency than direct body waves (e.g., Ben-Zion, 1990), we visually identify them as low-amplitude emergent first arrival signals with lower frequency and opposite polarity to the direct *P* arrivals. We also check the phase picks for nearby events to ensure consistency of the hand-picked arrivals.

To further verify the identified FZHW phases, we examine the polarizations of FZHWs and direct *P* waves on horizontal components (e.g., Bulut et al., 2012). Theoretically, the polarization of direct *P* wave is along the source–receiver direction. In contrast, FZHW radiates from the fault interface to the station located in the slower side. Hence, its polarization direction is oblique to the fault interface when arriving at that station. We use such differences in horizontal polarization to distinguish the phase arrivals of the FZHWs and direct *P* waves.

After phase picking, we obtain the travel time differences (Δt) or moveout between the FZHWs and direct *P* waves, and then estimate an average velocity contrast for a given station. Ben-Zion and Malin (1991) gives the relationship between the travel time difference (Δt) and the along-fault distance (r) as

$$\Delta t \sim r\left(\frac{1}{\alpha_2}-\frac{1}{\alpha_1}\right) \sim r\left(\frac{\Delta\alpha}{\alpha^2}\right), \tag{1}$$

where $\Delta\alpha$ and α denote the differential and average *P*-wave velocities, respectively. If we set the average velocity (α) for our study region to be constant, we can use the moveout data to estimate an average velocity contrast ($\Delta\alpha/\alpha$) along the fault interface by fitting the slope of the linear trend with Eq. (1).

4. Results

Among the 10 stations selected for analysis, station L6303 is located on the SW side of the GYF, and stations YS01, ys03, YUS and YS07 are located on the NE side. The remaining 5 stations (ys02, L6304, YS04, YS05 and YS06) are either on or very close to the surface rupture and previously mapped fault traces (Fig. 1), and hence are considered as fault zone (FZ) stations. A total of 49 020 waveforms produced by 1682 aftershocks are examined. The locations of 1248 events are obtained from a double difference relocated catalog (e.g., Wang et al., 2014). We use the catalog locations from China Earthquake Networks Center (CENC) for the remaining 434 events (Fig. 1).

After a systematic search, we identify FZHWs at 6 stations (ys02, L6304, ys03, YS04, YS05, YS06). We then check the waveforms and corresponding phase picks for all 10 stations to ensure consistency of the hand-picked arrivals (Fig. S1), and compare their horizontal polarizations with direct *P* waves to further confirm the observation of FZHWs (Figs. S2, S3). Finally, we pick arrival

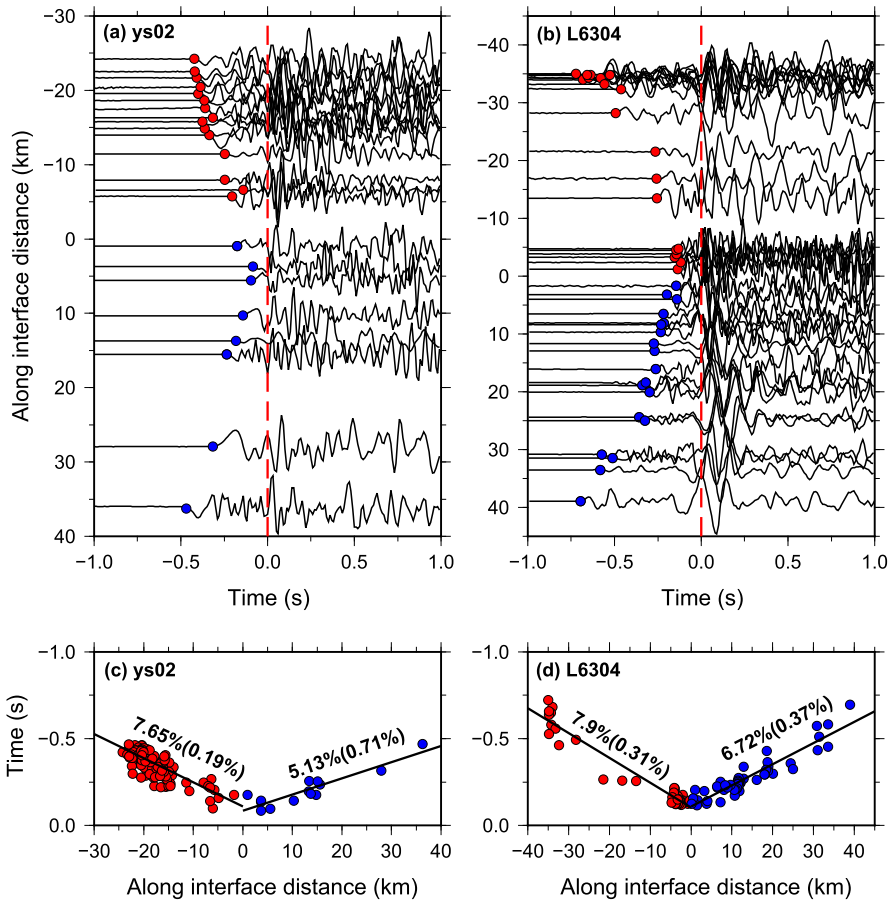

Fig. 2. Vertical seismograms recorded at stations ys02 (a) and L6304 (b) showing the moveout between FZHWs and direct *P* waves along the GYF. The red vertical dashed line marks the onset of the direct *P* wave, the red and blue dots mark the onset of FZHWs to the NW and SE along the GYF, respectively. (c–d) The corresponding differential arrival times between FZHWs and direct *P* waves versus the along-interface distances. The black solid lines show the least squares fitting of the data with the slope and 95 percent confidence bounds marked (For interpretation of the references to color in this figure legend, the reader is referred to the web version of this article.).

times of 485 FZHW phases as well as corresponding direct *P* phases. Among them, 234 and 97 events were recorded by stations ys02 and L6304, respectively. Waveforms and arrival times of both FZHWs and direct *P* waves recorded by stations ys02 and L6304 are shown in Fig. 2. After aligning the waveforms to the direct *P* arrivals, the FZHWs at these two stations show a rough linear relationship with along fault propagation distance.

To further estimate the average velocity contrast, we first apply a least-square fit to the data with Eq. (1). As was done before (e.g., Zhao and Peng, 2008; Zhao et al., 2010; Allam et al., 2014), we fit two slopes depending on whether the events occurred to the NW or SE sides of the station. Using the average *P*-wave velocity of 5.5 km/s (e.g., Liu et al., 2012; Wang et al., 2013), we estimate velocity contrasts at station ys02 to be ∼7.65% and ∼5.13% for events that occurred to the NW and SE sides, respectively. In comparison, the values at station L6304 are ∼7.9% and ∼6.72% for events on both sides, which are slightly larger than the values at station ys02. Additional examples of stations with and without FZHWs are shown in the online supplementary material (Figs. S4, S5).

To further confirm the robustness of our FZHW phase picks, we also apply a recently developed automatic FZHW picking program (e.g., Li and Peng, submitted for publication) to waveforms recorded at stations ys02 and L6304. As shown in Fig. S6, while the phase picks and numbers of FZHW observations are somewhat different, the general patterns and the estimated velocity contrasts are similar.

Fig. 3 shows the spatial distributions of measured time delays between the FZHWs and direct *P* waves for the 6 stations. The events that produced FZHWs are mainly clustered in two groups: one is from −40 to −25 km on the NW side of station ys02, and another is from −5 to 15 km beneath and on the SE side of station L6304. The focal depth is mainly above 12 km. In general, the time delays between the FZHWs and direct *P* wave increase with distance along the fault interface, suggesting the existence of a continuous bimaterial fault interface. However, we also observe clear spatial variability. For example, a cluster of events at −32 km distance produced up to 0.5 s time delays at station ys02. However, the same cluster of events only generated ∼0.3 s time delays at station ys03, although the along-strike distance for ys03 is nearly twice as long as ys02.

Such variability in time delay is summarized in Fig. 4a, which shows the average velocity contrasts for all 10 stations in the study region. In general, stations near the mainshock epicenter and to the NW side have larger velocity contrasts (5–8%) than stations to the SE (1–3%). Near the epicenter, velocity contrasts obtained from FZHW observations at stations ys02 and L6304 are larger than velocity contrasts observed at stations ys03 and YS04. In addition, stations on both sides of the pull-apart Jielong basin (e.g., stations ys02 and YS04 on the SW side, and stations L6304 and ys03 on the NE side) show evidence of FZHWs. However, stations that are further away (e.g., YS01, YS07, YUS and L6303) do not show any obvious evidence of FZHWs (Fig. S5). The coseismic slip mostly occurred on the SE side of the mainshock epicenter, and the maximum slip is up to ∼1.5 m (Fig. 4b). However, the largest velocity contrast (∼8%) is observed at station L6304 near the mainshock epicenter, and the velocity contrast is very small (less than 3%) at

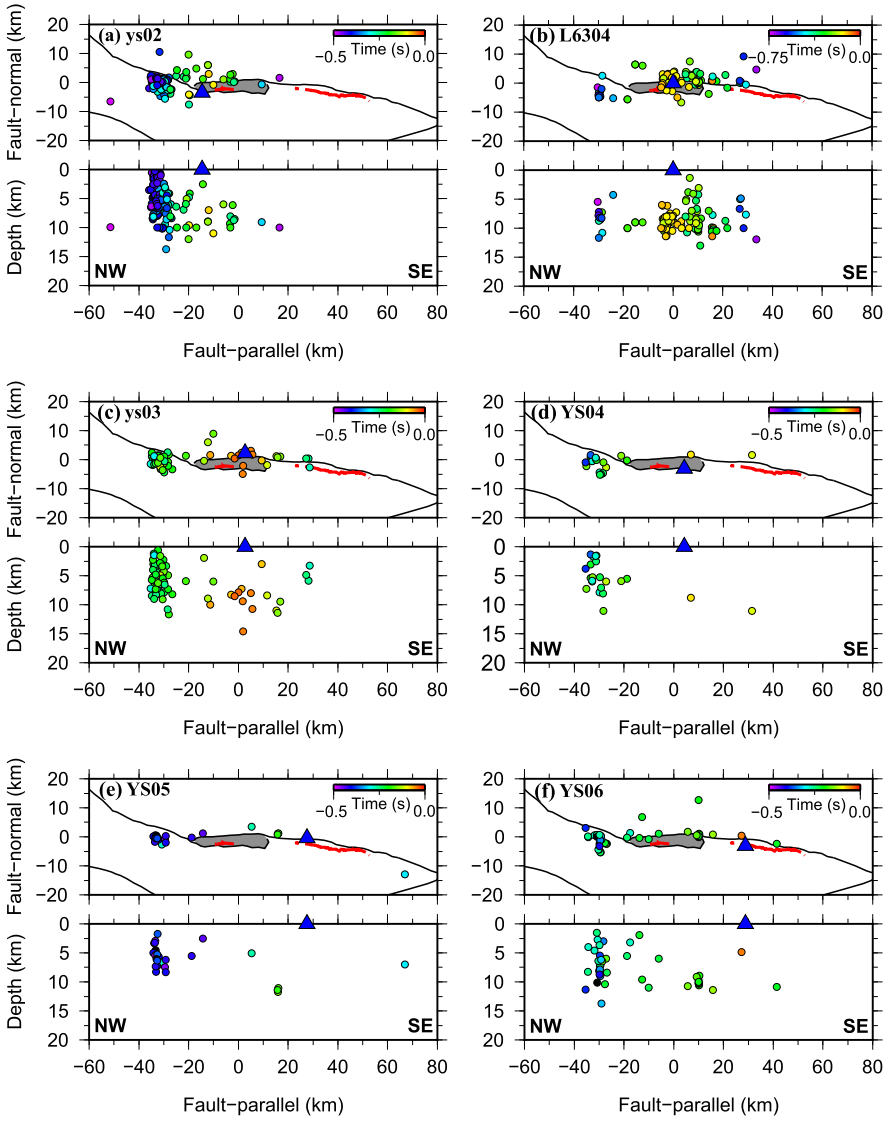

Fig. 3. A summary map-views and cross-sections with the event locations for the 6 stations that recorded FZHWs. The color of each hypocenter denotes the amplitude of the moveout between the FZHW and direct *P* wave. The events with FZHWs are mostly in the NW segment and near the mainshock epicenter, and their focal depths are mainly above 12 km (For interpretation of the references to color in this figure legend, the reader is referred to the web version of this article.).

stations YS05 and YS06 near the maximum coseismic slip zone. This indicates that the velocity contrast does not show any clear correlation with the mainshock slip.

Finally we also examine the relationships between the hypocentral depths and the time differences Δt (between the direct P waves and FZHWs). To remove the effects of along-strike variations, we only select events with epicentral distances less than 5 km of each station. As shown in Fig. 5, we do not observe any systematic changes of Δt with increasing hypocentral depth.

5. Discussion

We conducted a systematic study of FZHWs along the rupture zone of the 2010 Mw6.9 Yushu earthquake, and found clear along-strike variation in the percentage of velocity contrast. Relatively large velocity contrast on the order of 5–8% is observed at stations around the Jielong basin near the mainshock epicenter. In comparison, only 1–3% velocity contrast is observed SE of the epicenter along the Jiegu segment. The obtained values of velocity contrast is similar with those observed along major plate boundary faults, ranging from 5% to 10% along the Parkfield section of the SAF (e.g., Ben-Zion and Malin, 1991; Zhao et al., 2010), 3–12% along the Calaveras Fault (e.g., Zhao and Peng, 2008), 3–8% along the Hayward Fault (e.g., Allam et al., 2014), and ~6% along the NAF (e.g., Bulut et al., 2012).

Wang et al. (2013) conducted a tomographic inversion in the same region and found clear velocity contrasts extending to ~10 km depth in the NW part of the rupture zone (i.e., Jielong segment). They found that the *P* wave velocity in the Bayan Har block (NE) is up to 8% faster than in the juxtaposed Qiangtang block (SW). However, they did not find any clear velocity contrast in the SE part of the rupture zone (i.e., Jiegu segment). This is generally consistent with our observation of a lack of strong velocity contrast along the Jiegu segment. Recent field observations (e.g., Wang et al., 2008) also concluded that although the SE segment of the GYF marks a geomorphic boundary, the rocks on both sides are similar and primarily dark-green volcanic rocks mixed with greywacke of the Batang Formation.

Perhaps the most interesting observation of this study is that clear FZHWs were recorded at stations on both sides of the Jielong basin near the mainshock epicenter. Hence, our observations cannot be easily explained by a single bimaterial fault interface. As briefly mentioned before, the Jielong basin is a pull-apart basin that is bounded by two fault segments, and is currently filled by

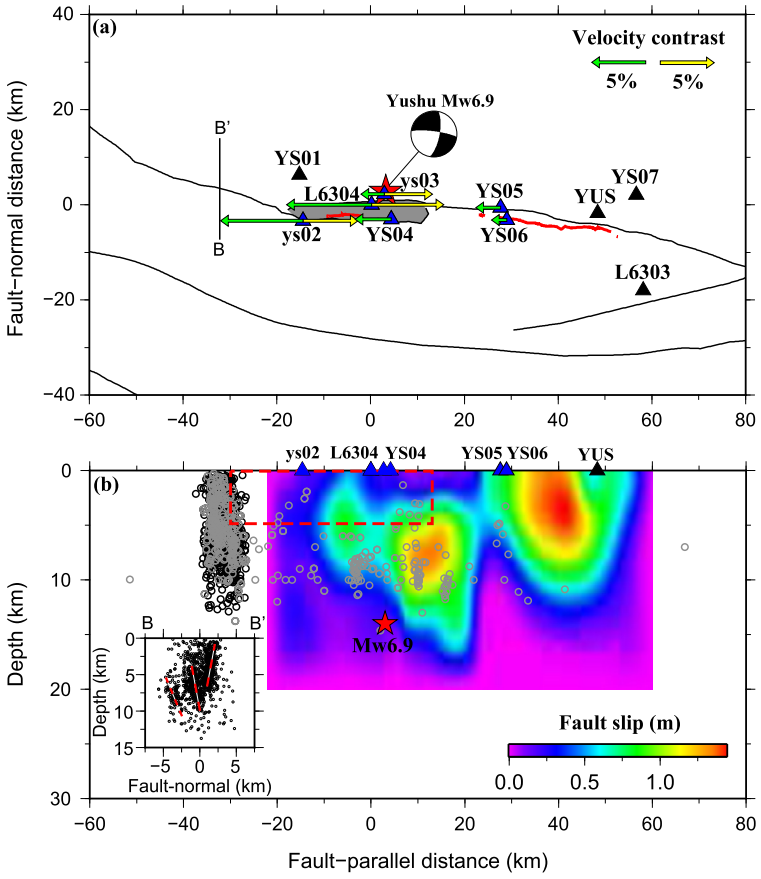

Fig. 4. (a) A summary map of the measured velocity contrasts for all stations with FZHWs along the GYF. The green and yellow arrows represent velocity contrast values for along-strike sections to the NW and SE that are centered at different stations, respectively. The length of each arrow is proportional to the percentage of the velocity contrast. Other symbols are the same as in Fig. 1. (b) The mainshock slip distribution along the GYF (e.g., Li et al., 2011). The red dashed rectangle marks a possible low-velocity zone (LVZ) formed beneath the Jielong basin, small gray circles denote hypocentral locations of aftershocks that generated FZHWs in this region, and the red star marks the hypocentral location of the Mw6.9 mainshock. The black and gray circles mark the relocated events (e.g., Wang et al., 2014) including with and without FZHWs. The inset shows a cross-section of seismicity from −26.5 km to −38.5 km along the GYF (or −6 km to 6 km projected at the center N:33.32°, E:96.23° with an azimuth of 23°). The red dashed lines mark possible evidence of a wedge-shaped structure outlined by the seismicity (For interpretation of the references to color in this figure legend, the reader is referred to the web version of this article.).

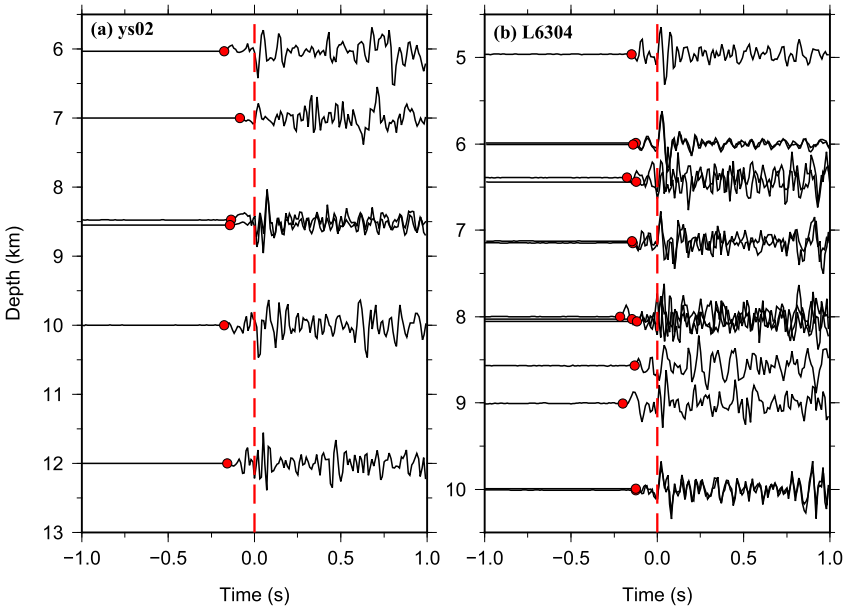

Fig. 5. Vertical seismograms recorded at stations ys02 (a) and L6304 (b) showing the lack of moveout between FZHWs and direct *P* waves with increasing hypocentral depths for events within 5 km of each station. The red dots and vertical dashed lines mark the onset of FZHWs and direct *P* waves, respectively (For interpretation of the references to color in this figure legend, the reader is referred to the web version of this article.).

the Longbao lake. It is quite possible that material beneath basin may include sediments or fractured material with water saturation, resulting a prominent LVZ, at least in the top few kilometers of crust. Wang et al. (2014) relocated the aftershocks using a double difference relocation algorithm, and found that aftershocks in our study region show a wedge-shaped distribution extending to seismogenic depth (Fig. 4b). In contrast, a detailed field study (e.g., Wang et al., 2008) before the 2010 Yushu mainshock revealed that the fault segment on the NE side of the basin is dipping ~50° to the SW. It juxtaposes the Neogene red beds in the footwall (SW) and Triassic, dark-green, volcaniclastic rocks in the hanging wall (NE). The pull-apart basin extends along the fault to the NW for at least 25 km, likely forms a wedge-shaped low-velocity zone (LVZ) between the Bayan Har (NE) and Qiangtang (SW) blocks, and produces two bimaterial interfaces near the basin boundaries. Stations located within or near the LVZ are expected to first record waves that refract along the faster block on either side or diffract from the bottom of the LVZ (e.g., Yang and Zhu, 2010), followed by direct P wave or P guided waves (e.g., Ellsworth and Malin, 2011) that propagate inside the LVZ. This is consistent with recent numerical simulations showing that material within fault stepovers remain damaged (i.e., with reduced rigidity and velocity) to larger depth through the entire seismic cycle (e.g., Finzi et al., 2009). We note that no clear increase of time difference Δt was found with increasing hypocentral depth (Fig. 5), suggesting that the LVZ likely exists only in the top few kilometers, rather than extending to the seismogenic depth.

An alternative structure for generating head waves is a horizontal interface near the Moho boundary or within the crust (e.g., Stein and Wysession, 2003). However, only stations on or very close to the fault trace recorded clear head waves, and we did not find any evidence of head waves at stations that are further away (e.g., YS01, YUS, YS07, and L6303). In addition, this would not produce the observed polarization that is skewed to the fault direction (Figs. S2, S3). In contrast, relatively simple waveforms are recorded at stations far away from the fault, indicating that complicated waveforms at FZ stations are not a source effect. Hence, the most probable structure is a vertical plane associated with the bimaterial fault interface, rather than a horizontal plane.

To further evaluate the interpretation of a shallow LVZ, we also examined the initial particle motion of the horizontal components for all events observed at the 6 stations in which FZHWs are observed. As shown in Fig. S7, the initial polarizations for several stations (ys02, ys03 and YS04) are not along the source–receiver or fault-strike directions, but are at distinct angles to the fault strike, indicating that the first arrivals propagate primarily in the surrounding blocks outside the LVZ. The pattern at station L6304 is less clear (Fig. S7). Hence, the polarization results are partially consistent with the LVZ interpretation.

Finally, the existence of a bimaterial fault interface is expected to affect many aspects of earthquake source properties, including generation of a preferred rupture direction in the slip direction of the slower block for a sub-shear rupture (e.g., Ben-Zion, 2001; Ampuero and Ben-Zion, 2008). For a super-shear rupture, the propagation direction is flipped (e.g., Weertman, 2002; Shi and Ben-Zion, 2006). Several recent studies have shown that the Mw4.7 foreshock, the Mw6.9 Yushu mainshock and the Mw6.0 aftershock nucleated around the Jielong basin (e.g., Lü et al., 2011). Detailed field investigation also confirmed that the 18 km surface rupture south of the Jielong basin was associated with the Mw6.0 aftershock (e.g., Li et al., 2012). Because the relative motion of the slower block (the Jielong basin) is to the NW, the NW propagation of the Mw6.0 aftershock is consistent with the preferred rupture direction. On the other hand, because the observed velocity contrast from the LVZ is most dominate in the top few kilometers of the crust, while most of the slip in that segment is below 5 km (e.g., Li et al., 2011), it is not clear whether the rupture direction is affected by the existence of LVZ or not.

The mainshock rupture propagated primarily to the SE, which appears to be consistent with the preferred rupture direction for a subshear rupture. However, the mainshock epicenter is to the NE of the dipping fault north of the Jielong basin, at a depth of 15–20 km (e.g., Lü et al., 2011). Hence, the dipping fault is unlikely the primary fault that ruptured near the epicenter. Stations YS05 and YS06 were situated on the previously mapped fault trace and the surface rupture of the Yushu mainshock, respectively. The inferred velocity contrast is 1–3%, and is mostly associated with aftershocks to the west of the Jielong basin (Fig. 3). In addition, recent seismic tomography (e.g., Wang et al., 2013) and surface mapping (e.g., Wang et al., 2008) in the same region also revealed that the velocity contrast along the primary surface rupture of the mainshock could be very small. Hence, FZHWs observed at these two stations could be mainly produced by the same LVZ that generated clear FZHWs at stations near the mainshock epicenter. If so, the LVZ would have to be extended to greater depths in order to affect the ray path (Fig. 3), which is inconsistent with the lack of increasing time difference with larger depth (Fig. 5). In summary, the initiation and main slip patch of Yushu mainshock (and its largest aftershock) do not appear to have a clear relationship with the bimaterial interface properties observed in this study.

The observations of FZHWs in this paper and Hough et al. (1994) suggest that many faults, not necessarily at plate boundaries, may produce FZHWs, as long as they juxtapose rocks of different properties. Additional studies are needed to better understand whether (or how) bimaterial fault interface properties affect earthquake rupture behaviors (e.g., Ampuero and Ben-Zion, 2008).

Acknowledgements

We thank the Data Management Centre of China National Seismic Network for providing the seismic data recorded by stations QH.YUS, L6303 and L6304 at Institute of Geophysics, China Earthquake Administration (e.g., Zheng et al., 2010), and the Instrument Centre of China Seismic Array, China Earthquake Administration, for providing data for the remaining temporary stations. The manuscript benefits from useful comments by Yehuda Ben-Zion, Chastity Aiken, Cliff Thurber, Hongfeng Yang, reviewer Marco Bohnhoff and editor Peter Shearer. This study was supported by National Natural Science Foundation of China (41222029) and the Yushu earthquake scientific investigation project. Z. Peng and Z. Li are partially supported by US National Science Foundation project EAR-0908310. Figures were generated using GMT (e.g., Wessel and Smith, 1998).

Appendix A. Supplementary material

Supplementary material related to this article can be found online at http://dx.doi.org/10.1016/j.epsl.2015.01.043.

References

Allam, A., Ben-Zion, Y., Peng, Z., 2014. Seismic imaging of a bimaterial interface along the Hayward fault, CA, with fault zone headwaves and direct P arrivals. Pure Appl. Geophys. 171, 2993–3011. http://dx.doi.org/10.1007/s00024-014-0784-0.

Ampuero, J.-P., Ben-Zion, Y., 2008. Cracks, pulses and macroscopic asymmetry of dynamic rupture on a bimaterial interface with velocity-weakening friction. Geophys. J. Int. 173, 674–692. http://dx.doi.org/10.1111/j.1365-246X.2008.03736.x.

Ben-Zion, Y., 1990. The response of two half spaces to point dislocations at the material interface. Geophys. J. Int. 101, 507–528.

Ben-Zion, Y., 2001. Dynamic ruptures in recent models of earthquake faults. J. Mech. Phys. Solids 49, 2209–2244.

Ben-Zion, Y., Malin, P., 1991. San Andreas fault zone head waves near Parkfield, California. Science 251, 1592–1594.

Bulut, F., Ben-Zion, Y., Bohnhoff, M., 2012. Evidence for a bimaterial interface along the Mudurnu segment of the North Anatolian Fault Zone from polarization analysis of P waves. Earth Planet. Sci. Lett. 327–328, 17–22. http://dx.doi.org/10.1016/j.epsl.2012.02.001.

Chen, L., Wang, H., Ran, Y., Sun, X., Su, G., Wang, J., Tan, X., Lin, Z., Zhang, X., 2010. The Ms7.1 Yushu earthquake surface rupture and large historical earthquakes on the Garzê–Yushu Fault. Chin. Sci. Bull. 55 (31), 3504–3509. http://dx.doi.org/10.1007/s11434-010-4-79-2.

Ellsworth, W., Malin, P., 2011. Deep rock damage in the San Andreas Fault revealed by P- and S-type fault-zone-guided waves. Geol. Soc. (Lond.) Spec. Publ. 359, 39–53. http://dx.doi.org/10.1144/SP359.3.

Finzi, Y., Hearn, E.H., Ben-Zion, Y.V., Lyakhovsky, 2009. Structural properties and deformation patterns of evolving strike-slip faults: numerical simulations incorporating damage rheology. Pure Appl. Geophys. 166, 1537–1573. http://dx.doi.org/10.1007/s00024-009-0522-1.

Guo, J., Zheng, J., Guan, B., Fu, B., Shi, P., Du, J., Xie, C., Liu, L., 2012. Coseismic surface rupture structures associated with 2010 Ms 7.1 Yushu earthquake, China. Seismol. Res. Lett. 83 (1), 109–118. http://dx.doi.org/10.1785/gssrl.83.1.109.

Hough, S.E., Ben-Zion, Y., Leary, P., 1994. Fault zone waves observed at the southern Joshua Tree earthquake rupture zone. Bull. Seismol. Soc. Am. 84, 761–767.

Lewis, M.A., Ben-Zion, Y., McGuire, J., 2007. Imaging the deep structure of the San Andreas Fault south of Hollister with joint analysis of fault-zone head and direct P arrivals. Geophys. J. Int. 169, 1028–1042. http://dx.doi.org/10.1111/j.1365-246X.2006.03319.x.

Li, Z., Peng, Z., submitted for publication. Automatic identification of fault zone head waves and direct P waves and its application in the Parkfield section of the San Andreas Fault, California. Geophys. J. Int.

Li, Z., Elliott, J., Feng, W., Jackson, J., Parsons, B., Walters, R., 2011. The 2010 Mw6.8 Yushu (Qinghai, China) earthquake: constraints provided by InSAR an body wave seismology. J. Geophys. Res. 116, B10302. http://dx.doi.org/10.1029/2011JB008358.

Li, C., Pang, J., Zhang, Z., 2012. Characteristics, geometry, and segmentation of the surface rupture associated with the 14 April 2010 Yushu earthquake, eastern Tibet, China. Bull. Seismol. Soc. Am. 102 (4), 1618–1638. http://dx.doi.org/10.1785/0120110261.

Liu, Q., Yang, Z., Xin, H., Li, Y., Sha, C., 2012. Relocation of Yushu Ms7.1 earthquake aftershocks and discussion on seismogenic structure. Chin. J. Geophys. 55 (1), 46–54.

Lü, J., Zheng, Y., Ma, Y., Wang, X., Shang, R., Su, J., Xiao, J., Zheng, B., 2011. Focal mechanisms and seismological structures of the Ms 4.7, Ms 7.1, and Ms 6.3 Yushu earthquakes of April 14, 2010. Prog. Geophys. 26 (5), 1600–1606. http://dx.doi.org/10.3969/j.issn.1004-2903.2011.05.012 (in Chinese).

McGuire, J., Ben-Zion, Y., 2005. High-resolution imaging of the Bear Valley section of the San Andreas Fault at seismogenic depths with fault-zone head waves and relocated seismicity. Geophys. J. Int. 163, 152–164. http://dx.doi.org/10.1111/j.1365-246X.2005.02703.x.

Najdahmadi, S., Bohnhoff, M., Bulut, F., Ross, Z., Ben-Zion, Y., 2014. Systematic imaging of bimaterial interfaces at the at the Karadere–Düzce segment of the North Anatolian Fault Zone, Turkey. In: 2014 AGU Fall Meeting. San Francisco, Calif., 15–19 December. Abstract T13C-4683.

Shi, Z., Ben-Zion, Y., 2006. Dynamic rupture on a bimaterial interface governed by slip-weakening friction. Geophys. J. Int. 165, 469–484. http://dx.doi.org/10.1111/j.1365-246X.2006.02853.x.

Stein, S., Wysession, M., 2003. An Introduction to Seismology, Earthquakes, and Earth Structure. Blackwell Publishing, Oxford, UK. 498 pp.

Wang, D., Mori, J., 2012. The 2010 Qinghai, China, Earthquake: a moderate earthquake with supershear rupture. Bull. Seismol. Soc. Am. 102 (1), 301–308. http://dx.doi.org/10.1785/0120110034.

Wang, S., Fan, C., Wang, G., Wang, E., 2008. Late Cenozoic deformation along the northwestern continuation of the Xianshuihe fault system, Eastern Tibetan Plateau. Geol. Soc. Am. Bull. 120, 312–327. http://dx.doi.org/10.1130/B25833.1.

Wang, C., Wu, J., Fang, L., Wang, W., 2013. The relationship between wave velocity structure around Yushu earthquake source region and the distribution of aftershocks. Chin. J. Geophys. 56 (12), 4072–4083. http://dx.doi.org/10.6038/cjg20131212 (in Chinese).

Wang, B., Yang, H., Peng, Z., Yang, J., Han, L., Yang, W., Yuan, S., Meng, X., 2014. High-resolution aftershock distribution of 2010 Mw6.9 Yushu, China earthquake and its implication. In: SSA 2014 Annual Meeting. Abstract.

Weertman, J., 2002. Subsonic type earthquake dislocation moving at approximately $\sqrt{2}\times$ shear wave velocity on interface between half spaces of slightly different elastic constants. Geophys. Res. Lett. 29 (10). http://dx.doi.org/10.1029/2001GL013916.

Wen, X., Xu, X., Zheng, R., Xie, Y., Wan, C., 2003. Average slip-rate and recent large earthquake ruptures along the Garzê–Yushu fault. Sci. China, Ser. D 33, 199–208.

Wessel, P., Smith, W.H.F., 1998. New, improved version of the Generic Mapping Tools released. Trans. Am. Geophys. Union 79, 579.

Xu, C., Xu, X., Yu, G., 2013. Landslides triggered by slipping-fault-generated earthquake on a plateau: an example of the 14 April 2010, Ms 7.1, Yushu, China earthquake. Landslides 10 (4), 421–431. http://dx.doi.org/10.1007/s10346-012-0340-x.

Yang, H., Zhu, L., 2010. Shallow low-velocity zone of the San Jacinto fault from local earthquake waveform modeling. Geophys. J. Int. 183, 421–432. http://dx.doi.org/10.1111/j.1365246X.2010.04744.x.

Yokota, Y., Kawazoe, Y., Yun, S., Oki, S., Aoki, Y., Koketsu, K., 2012. Joint inversion of teleseismic and InSAR datasets for the rupture process of the 2010 Yushu, China, earthquake. Earth Planets Space 64, 1047–1051. http://dx.doi.org/10.5047/eps.2012.04.008.

Zhang, G., Shan, X., Delouis, B., Qu, C., Balestra, J., Li, Z., Liu, Y., Zhang, G., 2013. Rupture history of the 2010 Ms 7.1 Yushu earthquake by joint inversion of teleseismic data and InSAR measurements. Tectonophysics 584, 129–137.

Zhao, P., Peng, Z., 2008. Velocity contrast along the Calaveras fault from analysis of fault zone head waves generated by repeating earthquakes. Geophys. Res. Lett. 35 (1), L01303.

Zhao, P., Peng, Z., Shi, Z., Lewis, M., Ben-Zion, Y., 2010. Variations of the velocity contrast and rupture properties of M6 earthquakes along the parkfield section of the San Andreas Fault. Geophys. J. Int. 180, 765–780. http://dx.doi.org/10.1111/j.1365-246X.2009.04436.x.

Zheng, X., Yao, Z., Liang, J., Zheng, J., 2010. The role played and opportunities provided by IGP DMC of China National Seismic Network in Wenchuan earthquake disaster relief and researches. Bull. Seismol. Soc. Am. 100 (5B), 2866–2872. http://dx.doi.org/10.1785/0120090257.

Zhou, R., Ma, S., 1996. Late quaternary active features of the Garzê–Yushu fault zone. Earthquake Res. China 12, 250–260 (in Chinese).